CROSS STREAM MIGRATION OF COMPLIANT CAPSULES IN MICROFLUIDIC CHANNEL

A Thesis

Presented to

The Academic Faculty

by

Alexander Kilimnik

In Partial Fulfillment

of the Requirements for the Degree

of Master of Science in the

School of George W. Woodruff School of Mechanical Engineering

Georgia Institute of Technology

May 2012

CROSS STREAM MIGRATION OF COMPLIANT CAPSULES IN MICROFLUIDIC CHANNEL

Approved by:

Dr. Alexander Alexeev, Advisor
George W. Woodruff School of
Mechanical Engineering
Georgia Institute of Technology

Dr. Todd Sulchek
George W. Woodruff School of
Mechanical Engineering
Georgia Institute of Technology

Dr. Minami Yoda
George W. Woodruff School of
Mechanical Engineering
Georgia Institute of Technology

Dr. Thorsten Stoesser
School of Environmental and Civil
Engineering
Georgia Institute of Technology

Date Approved: March 28, 2012

This work is dedicated to my amazing and supportive wife Becky and my daughter, Paige.

ACKNOWLEDGEMENTS

I am forever thankful for my advisor, Dr. Alexander Alexeev. He has provided invaluable guidance and mentorship. I wish to also thank my committee members, Drs. Todd Sulchek, Minami Yoda, and Thorsten Stoesser for taking the time out of their hectic schedules to review this work. I would also like to acknowledge the support, encouragement, and friendship of Hassan Massoud, Wenbin Mao, Chris Forster, and Jamie Huffman, and Rajat Ghosh. This effort would not be possible if it wasn't for the love and support I've received from my family.

TABLE OF CONTENTS

LIST OF FIGURES

SUMMARY

An understanding of the motion of soft capsules in microchannels is useful for a number of applications. This knowledge can be used to develop devices to sort biological cells on their size and stiffness. For example, cancer cells have different stiffness from healthy cells and thus can be readily identified. Additionally, devices can be developed to detect flaws in synthetic particles.

Using a 3D hybrid lattice Boltzmann and lattice spring computational method, the motion of rigid and soft capsules in a pressure-driven microfluidic flow was probed. The effect of inertial drift is evaluated in channels with different Reynolds numbers. Other system parameters such as capsule elasticity and channel size are also varied to determine their effect. The equilibrium position is also obtained.

The equilibrium position of rigid and soft capsules depends on the relative particle size. If the capsule is small, the equilibrium position is found to be closer to the channel wall. Conversely, for larger capsules, the equilibrium position is closer to the channel centerline. The capsule stiffness affects the magnitude of the cross-stream velocity. For a given Reynolds number, the equilibrium position of softer capsules is closer to the channel centerline. However, it is found that the equilibrium position of soft capsules is weakly dependent for Reynolds numbers 1-100.

CHAPTER 1

INTRODUCTION

1.1 Introduction & Motivation

Separation and sorting of particles and living cells has numerous applications in the areas of medical research, diagnostics, and treatment. Synthetic particles are being utilized for innovative methods for targeted drug delivery [2, 3]. The sorting of these particles is useful in identifying flaws in their preparation to assure the particle meets design tolerances. A common way of sorting cells and particles is within microfluidic flows [1, 4-6].

Microfluidic flows are actively used medical diagnostics methods such as flow cytometry. In flow cytometry, discussed further in Section 1.1, cells are suspended in a sheath fluid flowing in a microchannel and identified using a laser. When the cells are interrogated by the laser, the cells scatter the light and emit a fluorescence. This fluorescence is filtered and collected and the data is stored for further analysis by software. Microfluidic systems are typically characterized by their small channel size (up to 1000 μm) and flow volumes. However, the flow rate of these systems can be relatively high. For example, in flow cytometry, the flow rate can be up to 10 m/s [1].

While these methods are effective, there are limitations in the implementation. For example, the throughput in flow cytometry is limited by the serial nature of its design. Additionally, markers or stains may need to be added to the samples in order to facilitate detection [1].

The ability to distinguish cells by size and stiffness is useful in cell type identification. For example, the red blood cell and white blood cell counts are a common

metric gathered in blood testing. An indicator of stiffness could aid in the isolation of cancer and malaria cells in a sample [7-10].

In this thesis, an alternative method is presented for the marker less identification of cells and particles based on their size, stiffness, and the flow rate based on their position in a microchannel. Using computer-based models discussed in Chapter 2, the motion of rigid and soft particles is explored. Primarily, the equilibrium position of the particle is determined and related to the particle properties. The computational setup, validation, and results of simulations with a hybrid lattice-Boltzmann/Lattice Spring Model are discussed in Chapter 3. The effects of size, stiffness, and deformation are explored across a range of Reynolds numbers. Moreover, the size and stiffness can be used to hydrodynamically focus particles based on their position within the channel. Additionally, simulations involving droplets were performed in Chapter 4 and related to the results presented in Chapter 3.

1.1.1 Flow Cytometry

Flow cytometry is the measurement of various physicochemical characteristics of suspended cells. Cells suspended in a sheath fluid are subject to a flow in a capillary tube. The sheath fluid generally has a viscosity similar to water. The cross sectional sizes and flow velocities of the capillary tubes can range greatly [1]. For example, a cylindrical channel with a radius of 100 μm has approximately 1 m/s flow rate [1]. This translates to Reynolds number, an indicator of the relative importance of the inertial forces compared with the viscous forces, of 100. These cells are then hydrodynamically focused such that they flow past a laser in a single file. A schematic of flow detection is shown in Figure 1.1.

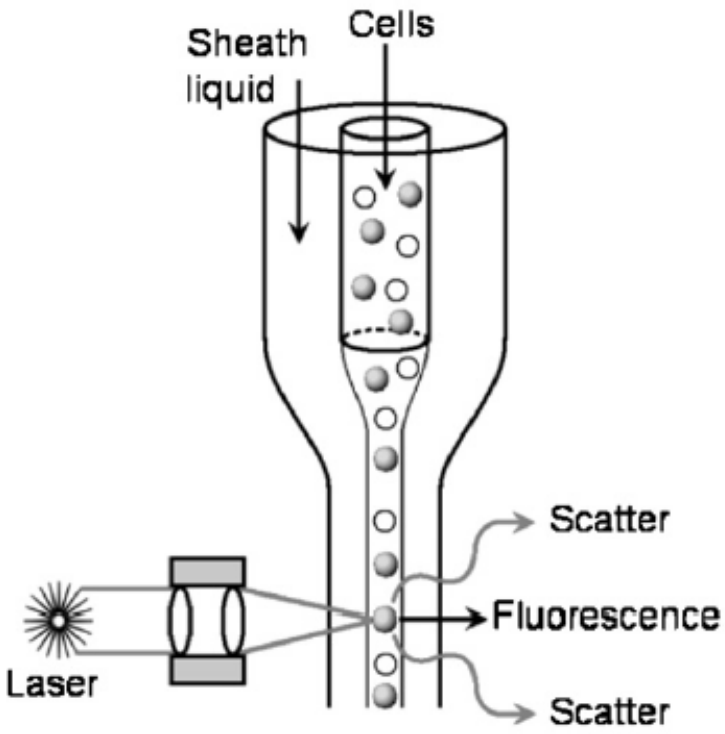

Figure 1.1. Schematic of sample detection in flow cytometry [1].

As each cell flows past the laser, they scatter the light at different angles and emit fluorescence. The combination of the angle and the fluorescence indicates properties of cell such as size, shape, cell surface markers, and other properties [1]. This method can be used to detect up to 25,000 cells per second.

While effective, this method of identifying cells does have some disadvantages. The cells must be hydrodynamically focused such that a single cell must be presented before the laser individually. Furthermore, the serial nature of the device limits the throughput in which cells can be interrogated. The preparation of cell samples can be burdensome. The process of cell preparation involves placing them through a centrifuge and the staining of samples using special stains which adds complexity and cost [11]. If an error is made in cell preparation, this can lead to false detections. Therefore, well-trained individuals are needed for both cell sample preparation and operating the

machine. Specialized training is necessary for the operation and interpretation of the results [12]. Furthermore, the cost of flow cytometers can be greater than $30,000 [13] not including cost of stains and preparation equipment.

A method to overcome some of these limitations is to utilize inertial drift (discussed in Section 1.2) to identify cells. Using inertial drift, the cells can be hydrodynamically separated based on their size and stiffness. Their position within the channel can be used to identify the cells based on their mechanical properties or size.

1.2 Background

This thesis explores the separation of particles using hydrodynamic effects within a microfluidic channel. These flows are typically operated in regimes where the Reynolds number is low which implies the viscous effects are stronger than the inertial effects acting upon the particle. Therefore, the inertial effects are commonly neglected in these regimes.

There have been a number of experiments and research [18-22] that imply that the inertial effects may not be neglected. Specifically, in the experiments carried out by Segre & Silberberg [14],[15], rigid polymethylmethacrylate spheres were released in an annulus and found to congregate in a distance of 0.63 of the channel radius. This experiment implies that there was the sphere migration due to inertial drift. Further discussion of the inertial drift effect is in Section 1.2.1.

The cause the particle equilibrium at 0.63 of the channel radius is due to a number of forces. The effect of the particle rotation is discussed in Section 1.2.2, but ultimately this influence does not dominate the particle motion. The reason particle equilibrates at the distance of 0.63 of the channel radius is primarily related to two effects. First, there is

a lift induced on the particle due to the fluid inertial driving the particle away from the center. This lift force is discussed further in Section 1.2.3. This lift force drives the particle towards the particle wall. When the particle approaches the wall, wall effects become dominant driving the particle towards the channel center. The wall effects are discussed further Section 1.2.4. At the point where these two effects are equally strong is where the capsule achieves an equilibrium position within the flow.

1.2.1 Segre & Silberberg Experiments

Segre & Silberberg ran experiments on polymethylmethacrylate spheres in suspensions. The spheres were released in a pipe of relatively low Reynolds numbers varying from 2 to 700. They explored various concentrations with volume fractions ranging from 0.005 to 0.068. When the spheres entered into the annulus, they were unordered. As the spheres progress downstream in the annulus, the concentration of sphere spiked at a position of about 63% of the annulus radius. The result from one of their samples is shown in Figure 1.2.

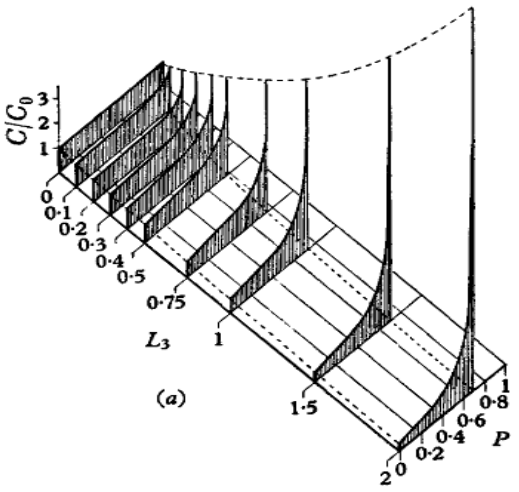

Figure 1.2. Sample data from Segre & Silberberg. Spheres enter an inlet in an annulus with no ordered concentration. Further downstream, the concentration is highest at 0.63.

They labeled this effect a tubular pinch. Additionally, they found that for Reynolds numbers greater than 30, the radial equilibrium position moved towards the pipe wall. This effect was later explored by Cox, Leal, and Matas [16-18] among others.

The effects observed by Segre & Silberberg can be caused by particle-particle interactions and particle-fluid interactions. If the particle concentration is high, this will induce a particle migration towards the channel centerline [19]. The particle-fluid effects due to inertia cause a lateral migration toward the wall. If the volume fraction of particles decreased to about 0.1, particle-fluid effects work in competition of the particle-particle effects causing the tubular pinch observed by Segre-Silberberg [18] .

1.2.2 Particle Rotation

In order to explain the phenomenon observed by Segre & Silberberg, numerical analysis and experiments were performed using rigid spherical particles. Rubinow & Keller [20] suggested that particle radial migration may occur due to the rotation of the particle as shown in Figure 1.3.

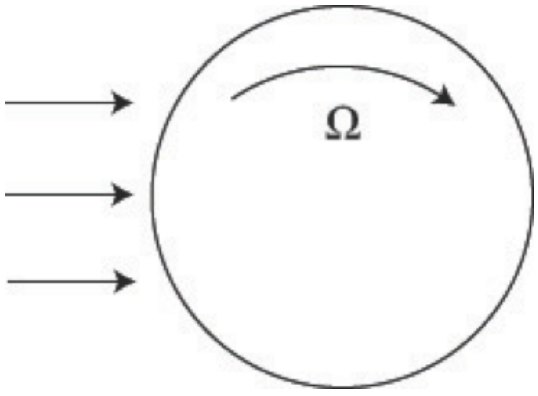

Figure 1.3. Illustration of particle rotation. The arrows represent a flow moving from left to right. The particle is rotating clockwise with angular velocity Ω.

Due to the rotation of the particle and the flow, the velocity relative to the particle on top is higher than that below it. This results in a lower pressure on the top of the particle and will induce a radial migration towards the channel centerline. Because Segre &

Silberberg observed radial migration away this explanation does not appear to be operative.

Another attempt to explain the radial velocity is that due to secondary flows induced by the presence of the particle itself. Cox & Brenner [16] developed a theory describing radial migration of both neutrally buoyant and non-neutrally buoyant spheres in tubes. In their analysis, they assumed that both the Reynolds and migration velocity are very small. They concluded that the inertial effects are not due to local effects associated with the body and that the migration speed is independent of rotation for neutrally buoyant particles.

1.2.3 Velocity Profile Curvature

One explanation the particle migrates towards the wall is due to the curvature of the velocity profile in the channel as shown in Figure 1.4. The parabolic velocity profile results in a force that pushes the particle away from the centerline of the channel toward the channel wall. At any given position in the parabolic profile, the fluid velocity near the centerline of the channel is always higher than that closer to the wall.

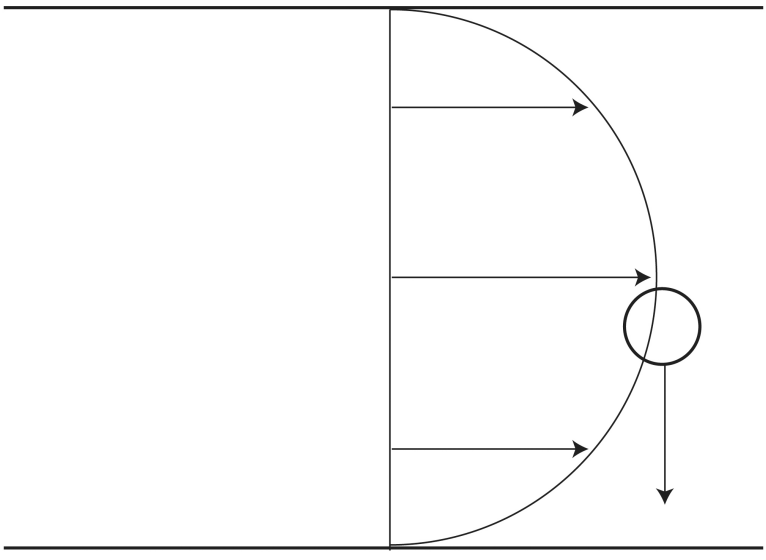

Figure 1.4. Illustration of parabolic velocity profile in channel with capsule.

However, the magnitude of fluid velocity relative to the particle is always higher closer to the channel wall as shown in Figure 1.5. The higher velocity towards the channel wall results in a lower pressure on the wall side of the particle. This lower pressure results in a force that drives the capsule towards the channel wall.

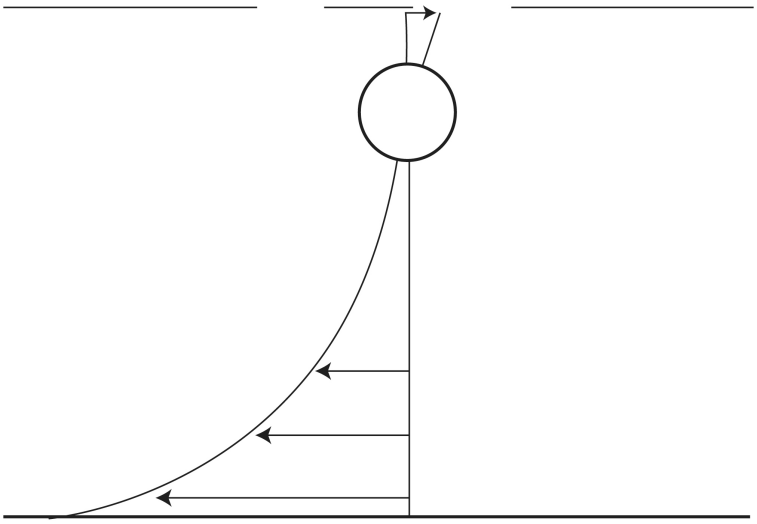

Figure 1.5. Flow velocity relative to capsule when far away from wall.

Segre & Silberberg noticed that the equilibrium position was at a distance of 0.63 of the tube radius away from the annulus centerline. If the curvature effects alone were the cause of the inertial migration, the particle would at some point come in contact with the channel wall. Thus, there is another effect that impacts the equilibrium position of the particle.

1.2.4 Wall Effects

Ho & Leal [21] further studied these phenomena both numerically and experimentally using neutrally buoyant rigid spheres in Couette and Poiseiulle flows. In their experiments, they observed two major effects. The first effect was observed experimentally where the rigid spheres were subject to simple shear in a Couette flow. They observed that the spheres migrated away from the wall due to the shear by the wall. Because of the presence of the wall, the flow slows down near the wall due to the no-slip

condition. This slowdown in velocity causes generates a pressure gradient forcing the particle away from the wall. The second effect was the outward force caused by the velocity profile illustrated in Figure 1.4. Consequently, a sphere within a 2D Poiseuille flow was found to achieve an equilibrium position near 0.6 of the channel half-height away from the channel centerline. Matas [18] later shows that the wall repulsive force is greatly reduced with increasing Reynolds number.

Thus, the cross-stream migration of particles is the result of two contributing effects. The first effect is due to the curvature of the velocity profile that moves the capsule toward the channel wall. The other is a force, which pushes the particle away from the wall. When these contributions are equal, there is no net lift force on the particle in the direction normal to the stream flow. This results in a zero cross-stream drift velocity and the particle is in a stable equilibrium position.

Schonberg & Hinch [22] performed a mathematical analysis of a sphere in Poiseuille flow. In their computation, they used characteristic lengths shown in Figure 1.6.

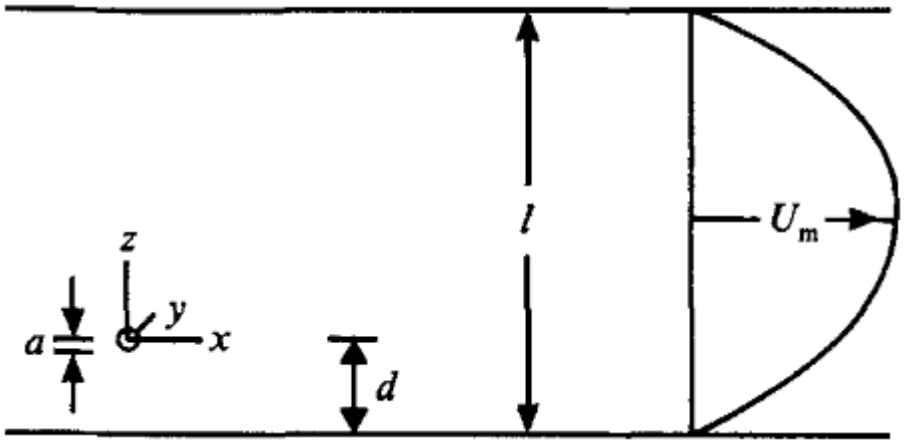

Figure 1.6. Channel dimensions for Schonberg & Hinch [22].

Two parameters that Schonberg and Hinch used to define their system were the Reynolds number based off the channel height and the particle Reynolds number. They are,

$$\mathrm{Re} = \frac{U_{\max}\ell}{\nu} \tag{1}$$

$$\mathrm{Re}_p = \frac{U_{\max}a^2}{\nu\ell} \tag{2}$$

They considered a case where the sphere can both translate and rotate. Schonberg and Hinch found that the lateral migration velocity of the sphere is

$$W_p = \frac{a}{l}\mathrm{Re}_p\,\mathrm{Re}\int_{-\infty}^{\infty}\int_{-\infty}^{\infty} W_0(k_1,k_2,0)dk_1dk_2 \tag{3}$$

where

$$W_0(k_1,k_2,Z) = \frac{1}{4\pi^2}\int_{-\infty}^{\infty}\int_{-\infty}^{\infty} U_0(X,Y,Z)e^{-i(k_1X+k_2Y)}dXdY \tag{4}$$

Using these results, they plotted the migration velocity for the spheres at channel Reynolds numbers of 1, 75, and 150 shown in Figure 1.7. Schonberg compared the results to experiments and found good agreement. Their data were used in the validation of our computational model.

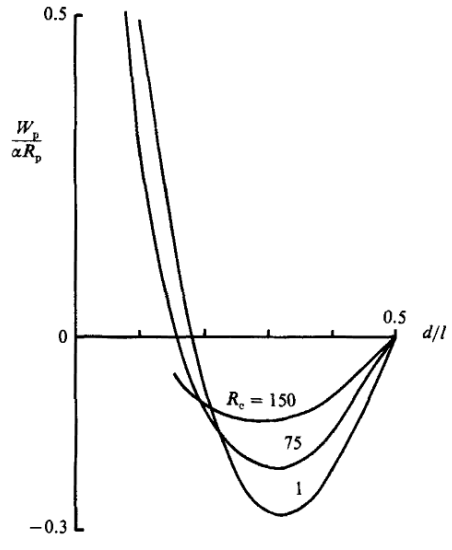

Figure 1.7. Particle migration velocity as a function of position for different Reynolds numbers. Analytical results produced by Schonberg & Hinch [22].

The above research suggests that the inertial migration of a particle has a dependency on the particle size. However, none of these analyses address the case where the particles are soft and free to deform. The effect of deformation of small particles is explored in this thesis in chapter 3. The knowledge of how inertial migration is affected by such system characteristics as the Reynolds number, particle size, and particle deformability (in the case of elastic particles) can be used to develop particle and cell separation devices [4].

CHAPTER 2

METHODOLOGY

Using computer-based simulations, the motion of rigid and soft particles is modeled. These physic-based numerical models predict specific aspects of the system. The hydrodynamic interaction is modeled using a lattice-Boltzmann model (LBM). The lattice-Boltzmann Model is discussed in Section 2.1. The capsule is modeled a network harmonic springs using the Lattice Spring Method (LSM) discussed in Section 2.2. The LSM is used to simulate the rotation and deformation of the capsule encapsulated in the fluid modeled by the LBM. These two numerical models are coupled together to accurately simulate the interaction of the fluid on the particle, and vice versa. The coupling of the LBM is discussed further in Section 2.3. This hybrid LBM/LSM model is incorporated in the simulation performed in Chapter 3 that simulates the capsule motion throughout a range of microchannels. Furthermore, the stiffness of the capsule is varied to determine the impact of the deformation on the motion of the capsule. Finally, droplets are simulated using a Binary LBM discussed in Section 2.4.

2.1 Lattice-Boltzmann Method (LBM)

One of the core techniques of the simulation environment in this study is the Lattice Boltzmann method (LBM). This method is used to simulate the hydrodynamic interactions among solid particle, channel walls and a viscous fluid using a set of density distribution functions describing microscopic “fluid particles”. Cumulatively, these microscopic interactions govern the behavior observed on the macroscopic scale. Since simple microscopic behavior is modeled, simulations of complex environments can be carried out with reduced computational effort compared to traditional methods.

Furthermore, the LBM can be easily parallelized and can handle complex geometries. Thus, this method constitutes an efficient solver for the Navier-Stokes equations in complex geometries.

The microscopic behavior modeled via collision and propagation of fluid particle distributions at each discrete location in space (node). At each time step, fluid particles enter a node, collide, and propagate as shown in the in Figure 2.1

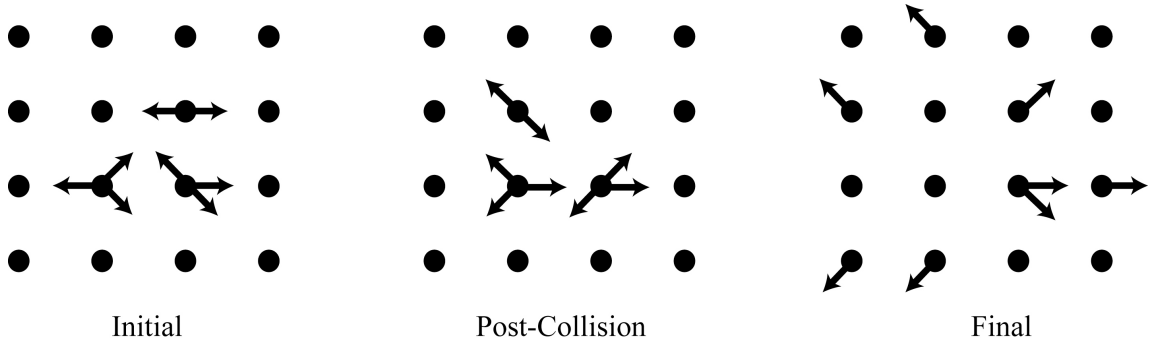

Figure 2.1. Capsule propagation, collision, and final steps.

The evolution of this behavior is governed by the discretized lattice Boltzmann equation [23]. In this equation, the local distribution function, $f_i(r,t)$, is propagated across each lattice vector $\vec{c}_i$ at each time step Δt. The right hand of the expression, describes the collision operation. The collision step is linearized with a single relaxation parameter τ. The final term is the equilibrium distribution function f_i^0.

$$f_i(r+\vec{c}_i\Delta t, t+\Delta t) - f_i(r,t) = -\frac{1}{\tau}(f_i - f_i^0) \tag{5}$$

By taking the moments of the capsule distribution function $f_i(r,t)$, we obtain the mass density, momentum density, and momentum flux defined by (6-8). The variable $\vec{u}$ represents the local fluid velocity at each node.

$$\rho = \sum f_i \tag{6}$$

$$j = \rho\vec{u} = \sum f_i \vec{c}_i \tag{7}$$

$$\Pi = \sum f_i \vec{c}_i \vec{c}_i \tag{8}$$

At each node, the local distribution function is totaled across all the possible directions the fluid capsules can move. The equilibrium distribution function is:

$$f^0 = a^{c_i}\left[\rho + \frac{\vec{j} \bullet \vec{c}_i}{c_s^2} + \frac{\rho\vec{u}\vec{u} : (\vec{c}_i\vec{c}_i - c_s^2\vec{1})}{2c_s^4}\right] \tag{9}$$

The coefficient a^{c_i} is used to compensate for the fact that, for each time step, particles propagating to nodes at 45 degrees travel a greater distance than those that propagate to nodes at 0, 90, 180, and 270 degrees. In each direction (*i*), appropriate values of the coefficient *a* are:

$$a^0 = \frac{1}{3} \tag{10}$$

$$a^1 = \frac{1}{18} \tag{11}$$

$$a^{\sqrt{2}} = \frac{1}{36} \tag{12}$$

By taking moments of the local equilibrium distribution function, we obtain the following relationships.

$$\sum f_i^0 = \rho \tag{13}$$

$$\sum f_i^0 \vec{c}_i = \rho\vec{u} \tag{14}$$

$$\sum f_i^0 \vec{c}_i \vec{c}_i = P\vec{1} + \rho\vec{u}\vec{u} \tag{15}$$

The equation of state that defines P is as follows. The adiabatic speed of sound, c_s, is equal to $\sqrt{(c^2/3)}$.

$$P = \rho c_s^2 \tag{16}$$

The viscosity of the fluid is governed by the relaxation parameter. In order to maintain numerical stability of the system, the kinematic viscosity ν must be below $\Delta x^2/\Delta t$. The kinematic viscosity of the fluid is given by:

$$\nu = \frac{1}{6}\left(\frac{2}{\tau} - 1\right) \tag{17}$$

2.2 Lattice Spring Method (LSM)

The lattice spring method (LSM) is utilized to model the neutrally buoyant compliant capsule. An elastic solid is modeled using a network of harmonic springs that are connected across nodes of equal spacing. The energy associated with each node at position r_i is:

$$E_s = \frac{1}{2}\sum_i k(r_{ij} - r_{ij}^{eq})^2 \tag{18}$$

In the above equation, r_{ij} is the magnitude of the distance between the nodes *i* and node *j*. The equilibrium distance between nodes is represented by r_{ij}^{eq}. The variable k represents the spring constant. The total force acting on each node is

$$F_s = -\sum_i k\left(\frac{r_{ij} - r_{ij}^{eq}}{r_{ij}}\right) \bullet r_{ij} \tag{19}$$

The system dynamics are captured by integrating Newton's equation of motion using the velocity Verlet algorithm.

$$F = M_i \frac{\partial^2 r_i}{\partial t^2} \tag{20}$$

To integrate this equation, we first calculate the total force, which is comprised of both the spring force and the force exerted by the fluid, for each node. The mass of each node is represented M_i.

The neutrally buoyant capsule's spherical shell is constructed from two concentric layers of LSM nodes. The nodes are distributed across each layer using the Delaunay triangulation technique. A distance Δx_{LS} that is equal to the average length of a triangular bond separates the surfaces. They are connected by springs between the nearest and next nearest neighbor nodes. The solid density is given by ρ_c:

$$\rho_c = \frac{2M_i}{\sqrt{3}\Delta x_{LS}^3} \tag{21}$$

Important physical properties such as Young's modulus, E, and the speed of sound need to be further stated to quantify in the system. The Young's modulus of the shell can be approximated by,

$$E = \frac{5k}{2\Delta x_{LS}} \tag{22}$$

and the speed of sound is given by,

$$c_s = \Delta x\sqrt{\frac{3k}{M}} \tag{23}$$

In order to maintain stability in the system, appropriate values for the time step and node spacing need to be selected. The Courant number, Cr, governs the stability of the system. A stable system has a Courant number of less than one.

$$Cr = \frac{c_s \Delta t}{\Delta x_{LS}} \tag{24}$$

To avoid large fluctuations in the fluid force, the lattice spring node spacing, Δx_{LS}, is set larger than the lattice Boltzmann node spacing, Δx.

2.3 LBM/LSM Coupling

When undergoing motion, forces due to the hydrodynamic interactions with the viscous fluid influence the solid capsule. The hydrodynamic forces are due to the fluid pressure and viscous stresses. At each surface node, the force due to the moving solid must be applied to the fluid, and conversely, the fluid forces must be applied to the lattice spring nodes. This is performed in a sequential manner beginning with resolving the lattice spring method and then the lattice Boltzmann method.

In the initial step, the lattice spring method is employed while applying the forces acting on the LSM nodes due to the springs and surrounding fluid. The node positions and velocities are determined by solving Newton's equations of motion using the Verlet algorithm. Thus, the velocities of the nodes along the solid/fluid interface are determined. Using these velocities, a bounce-back boundary condition is applied and the propagation step for the lattice Boltzmann method is run on the fluid. The final step of the lattice Boltzmann method, collision, is computed and the entire process repeats again.

The fluid particle distributions that are affected by the solid surface are subject to a "link" bounce back boundary condition [23]. This method is of second order accuracy [23]. A link is a path from a LBM node to a surface connecting neighbor LSM nodes, which cuts the link. The fluid interacts with the solid at nodes placed between the lattice Boltzmann node as shown in the following figure. The quantities d, and r_2 are defined by

$$d = \left|\mathbf{r}_1 - \mathbf{r}_b\right| / \left|\mathbf{r}_1 - \mathbf{r}_2\right| \tag{25}$$

$$\mathbf{r}_2 = \mathbf{r}_1 + \mathbf{c}_i \Delta t \tag{26}$$

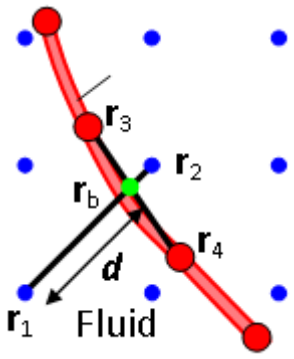

Figure 2.2. Illustration of interpolation bounce back boundary rule.

The node at which the fluid originates is defined to be r_1. For d=1/2, these fluid particles will arrive back at node r_1 after precisely one time step with a velocity that is opposite in direction to their original velocity. However, when $d \neq 1/2$, fluid particles will end up at positions that do not coincide with a regular lattice node and some sort of interpolation is needed[24]. We follow the interpolation scheme that was developed by Bouzidi et al. [25]

Specifically, for $d < 1/2$ we apply the following boundary rule that accounts for the component of the boundary velocity in the direction of the fluid capsule's velocity

$$f_k(\vec{r}_1, t+\Delta t) = (1-2d) f_i^*(\vec{r}_1 - \vec{c}_i \Delta t, t) + 2d f_i^*(\vec{r}_1, t) - \frac{2\alpha_i}{c_f^2} \rho(\vec{r}_1, t) \vec{c}_i \cdot \vec{u}_b(\vec{r}_b, t) \tag{27}$$

When $d > 1/2$, we calculate a new distribution after it is bounced from the solid as follows

$$f_k(\vec{r}_1, t+\Delta t) = \frac{2d-1}{2d} f_k^*(\vec{r}_1, t) + \frac{1}{2d} f_i^*(\vec{r}_1, t) - \frac{\alpha_i}{d c_f^2} \rho(\vec{r}_1, t) \vec{c}_i \cdot \vec{u}_b(\vec{r}_b, t) \tag{28}$$

Here, the subscript k stands for fluid particles with a velocity in the opposite direction of the incoming particles, i.e. $\vec{c}_k = -\vec{c}_i$. The velocity $\vec{u}_b$ is obtained through a linear interpolation between the velocities of the LSM nodes near the intersection point. This scheme conserves the mass and momentum with second order accuracy and yields a no-slip boundary condition at the solid-fluid interface.

As a result of the bounce-back process, the fluid exerts a force on the solid. This force is taken to be equal to the rate of exchange in momentum that takes place as the fluid particles are reflected at the interface, i.e.,

$$\vec{F}_b\left(\vec{r}_b, t+\tfrac{1}{2}\Delta t\right) = \left\{\left[f_i^*\left(\vec{r}_1,t\right)-\alpha_i\rho\left(\vec{r}_1,t\right)\right]\vec{c}_i - \left[f_k\left(\vec{r}_1,t+\Delta t\right)-\alpha_i\rho\left(\vec{r}_1,t\right)\right]\vec{c}_k\right\}\frac{\Delta x^3}{\Delta t} \tag{29}$$

The terms $\alpha_i\rho\left(\vec{r}_1,t\right)$ compensate for the ambient pressure, ensuring that the force on the interface is zero when the entire system is at rest. The force $\vec{F}_b$ is distributed as a load to the neighboring LSM nodes, while conserving the normal and tangential force on the fluid-solid interface.

2.4 LBM for Binary Fluids

There are several methods for applying the lattice Boltzmann method to binary fluids [26-32]. The primary difference between models is in the collision step. The models can be modified to adjust for large density ratios and other characteristics in the flow. In this study, we model neutrally buoyant droplets in a shear flow. For these simulations, the single fluid LBM model described in the previous section can be effectively expanded to capture the hydrodynamics of binary fluids using a free energy model. As such, a energy-based binary LBM model was selected [28].

To extend the lattice Boltzmann method for binary fluids, additional terms must be introduced. First, the distribution function for two species, A and B, has to be quantified. Second, the attraction between the two fluids needs to be modeled in order to best approximate the interaction between the two fluid species. Finally, the pressure must be quantified for a mixed fluid.

Certain characteristics of the binary fluid are required to model this environment. The mass densities of the each of the two fluid species is represented by ρ_A and ρ_B. The

local mass density is defined as (30). The local order parameter ϕ is defined in equation (31).

$$\rho(r,t) = \rho_A + \rho_B \tag{30}$$

$$\phi(r,t) = \rho_A(r,t) - \rho_B(r,t) \tag{31}$$

The two fluid species and their interface are quantified using the free energy functional,

$$F = \int dr\left(\psi + \frac{\kappa}{2}\left|\nabla\phi\right|^2\right) \tag{32}$$

Where free energy density $\psi(\phi)$ is defined by,

$$\psi = \rho c_s^2 - \ln\rho - \frac{a_{LBB}}{2}\varphi^2 + \frac{b_{LBB}}{4}\varphi^4 \tag{33}$$

In the expression above, the parameters a_{LBB}, $b_{;LBB}$, and κ are used to define the interfacial tension and thickness. The values of $b_{;LBB}$, and κ must be positive. The value of a_{LBB} is used to define whether the system is homogeneous or multiphase where a negative value indicates a homogenous system. In a multiphase system, the local order parameter will approach an equilibrium value of $+\phi_0$ and $-\phi_0$. The equilibrium value is determined by,

$$\varphi_0 = \sqrt{\frac{a_{LBB}}{b_{LBB}}} \tag{34}$$

Finally, the interface thickness (ξ) and the surface tension (σ) are given by,

$$\xi = 5\sqrt{\frac{\kappa}{2a_{LBB}}} \tag{35}$$

$$\sigma = \sqrt{\frac{8\kappa a_{LBB}^3}{9b_{LBB}^2}} \tag{36}$$

Similar to the single fluid LBM, the overall process involves collision and propagation and is captured using a discretized Boltzmann equation. However, with the introduction of a second fluid, a second equation is required. Instead of a separate function for each fluid species, the equations are given in terms of total mass density ρ_i and the order parameter ϕ_i. They are,

$$\rho_i = (t + c_i\Delta t, t + \Delta t) = \rho_i(r,t) - \frac{1}{\tau_\rho}\left(\rho_i(r,t) - \rho_i^{eq}\right) \tag{37}$$

$$\phi_i = (t + c_i\Delta t, t + \Delta t) = \phi_i(r,t) - \frac{1}{\tau_\phi}\left(\phi_i(r,t) - \phi_i^{eq}\right) \tag{38}$$

The equilibrium distributions for total mass density and the order parameter are represented by ρ_i and ϕ_i, respectively. The first relaxation parameter, τ_ρ, is used to determine the shear viscosity of the fluid. It is given by,

$$\eta = \rho c_s^2\left(\tau_\rho - \frac{1}{2}\right) \tag{39}$$

A second relaxation parameter τ_ϕ is introduced for the local order parameter. The values of τ_ϕ and τ_ρ were set equal for all the simulations. As with the single fluid LBM, c_i represents the local velocity the node direction *i*. The equilibrium distributions when *i*=0 (fixed) are,

$$\rho_0^{eq} = \rho - \sum_{i\neq 0}\rho_i^{eq} \tag{40}$$

$$\phi_0^{eq} = \phi - \sum_{i\neq 0}\phi_i^{eq} \tag{41}$$

Otherwise, they are defined by,

$$\rho_i^{eq} = a_i\left(A + \frac{\rho\vec{u}\phi_i \cdot \vec{c}_i}{c_s^2} + \frac{\left(\rho\vec{u}\vec{u} + \kappa\nabla\phi\nabla\phi\right):\left(c_i c_i - c_s^2\vec{I}\right)}{2c_s^4}\right) \tag{42}$$

$$\varphi_i^{eq} = a_i\left(\frac{\Gamma_{LBB}\mu}{c_s^2} + \frac{\varphi\vec{u}\cdot\vec{c}_i}{c_s^2} + \frac{\left(\varphi\vec{u}\vec{u}\right):\left(c_i c_i - c_s^2\vec{I}\right)}{2c_s^4}\right) \tag{43}$$

where $\vec{I}$ is the identity matrix and A is given by,

$$A = \frac{1}{c_s^2}\left(p_0 + \kappa\phi\nabla^2\phi - \frac{1}{2}\kappa\left|\nabla\phi\right|^2\right) \tag{44}$$

For i≠0, $\vec{u}$ represents the fluid velocity, μ represents the chemical potential, and Γ_{LBB} is a coefficient related to the mobility. The mobility is defined by,

$$M = \frac{\Gamma_{LBB}\left(2\tau_\varphi - 1\right)}{2} \tag{45}$$

Mobility controls the strength of diffusion. Setting the correct mobility is crucial to obtaining realistic results in the simulations. At each time step, the two fluids interact and diffuse through the interface and achieve equilibrium. The mobility number must be set such that the interface relaxes to equilibrium within each time step. If the mobility number is too high, residual diffusion will improperly affect the results. If the value is too low, the interface will not achieve equilibrium by the end of the time step. The mobility number was chosen using verified values by Kendon [33].

Figure 2.3 shows a droplet formed by fluid A (shown in blue) with a value of -1. The outer fluid 2 (shown in red) has a value in -1. The region where the value changes from -1 to 1 is the interface region.

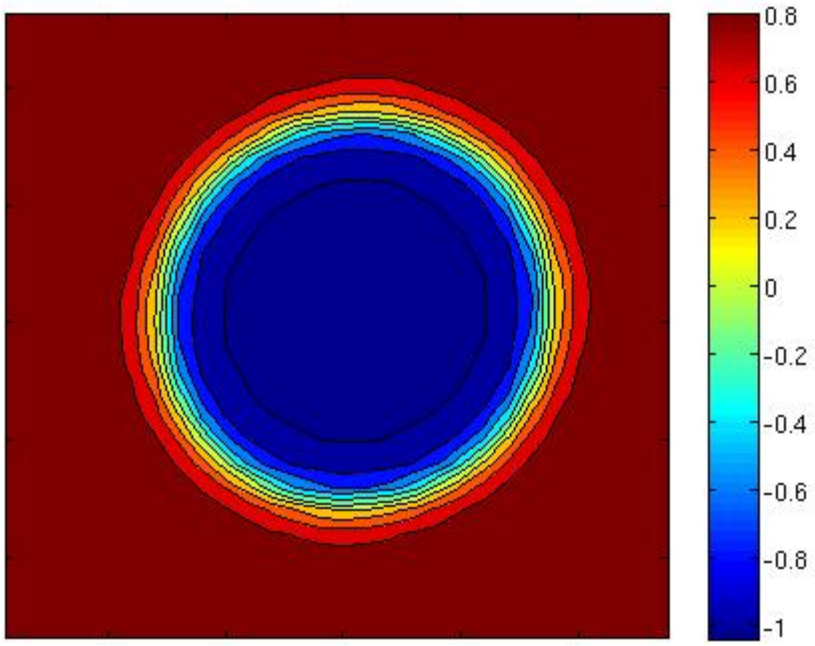

Figure 2.3. Droplet modeled using binary lattice-Boltzmann method. The red region is fully saturated with fluid A and has a value of 1. The blue region is saturated with fluid B and has a value of -1.

The final terms needed to resolve the system are the chemical potential energy, μ, and the pressure tensor $\vec{P}$,

$$\mu = \frac{\partial \psi}{\partial \phi} - \kappa \nabla^2 \phi \tag{46}$$

$$\vec{P} = p_0 \vec{I} + \kappa \left[\nabla \phi \nabla \phi - \left(\phi \nabla^2 \phi + \frac{1}{2} |\nabla \phi|^2 \right) \vec{I} \right] \tag{47}$$

Where,

$$p_0 = \rho \frac{\partial \psi}{\partial \phi} + \phi - \psi \tag{48}$$

CHAPTER 3

NEUTRALLY BUOYANT SOLID CAPSULE

In an effort to explore the impact of different mechanical properties on cells and synthetic particles, simulations were performed using the methodology described in Chapter 2. Specifically, the effect of the capsule size and compliance on cross-stream inertial drift is explored to acquire the particles position within the channel. These cells and particles were modeled as neutrally buoyant fluid-filled capsules that are spherical when they are not deformed. The capsules are modeled using LSM while the fluid is modeled using LBM. We specifically probe the effect of capsule size and compliance on the cross-stream inertial drift and equilibrium position. The background behind the domain size and characteristics is discussed in Section 3.1. The computational setup and model validation is described in further detail in Sections 3.2 and 3.3, respectively. The result obtained from the simulations is discussed in Section 3.4 and the proof of concept is discussed in Section 3.5.

3.1 System Parameters

In order to sort cells by size and stiffness, the mechanical properties of cells must be known. The cell types that will be considered are red blood cells (RBCs) and white blood cells (WBCs). The mechanical properties of RBCs have typically been explored using micropipette experimentation. These experiments have shown that the elastic shear modulus of RBCs are approximately 0.01 dyne/cm [34]. The diameter of a human RBC is approximately 8 μm.

White blood cells have different mechanical properties and are larger than RBCs. While there are several different types, the most commonly occurring is the neutrophil.

The neutrophil is typically between 10-12 μm in diameter. The tensile modulus of neutrophils is approximately 0.024±0.003 dyne/cm [35].

When composing the system, appropriate channel dimensions were selected for the sorting of capsules. A channel height of 100 μm [1] is appropriate for capsule sorting. When utilizing a channel height 100 μm, this leaves a ratio of the channel height to cell size of approximately 10. The flow rate for this configuration is approximately 0.1 m/s. Assuming the sheath fluid has properties similar to water, the Reynolds and capillary numbers for this system are,

$$\mathrm{Re} = \frac{U_{\max} H}{\nu} \sim 10 \tag{49}$$

$$\mathrm{Re}_p = \frac{U_{\max} a^2}{\nu H} \sim 0.1 \tag{50}$$

$$Ca = \frac{\mu U_{\max} 2a}{EhH} \sim 1 \tag{51}$$

Where $U_{\max}$ is the maximum flow velocity, H is the channel height, E is the Young's Modulus, h is the shell thickness, and a is the capsule radius.

3.2 Computational Setup

The simulation environment consists of a fluid filled neutrally buoyant capsule with radius R placed within a micro-channel. The microchannel has a solid horizontal wall placed at the y=0 position. A second solid wall is placed at a position y=H where H signifies the channel height. There are no walls along the x- and z-direction and a periodic boundary condition is placed at the boundaries of each of x- and z-direction boundaries. The computational domain size was set such that the length (x-direction) was 50a, width (z-direction) was 2H, and the height (y-direction) was varied. This domain

size is shown to be valid in Section 3.3.2. A pressure gradient is applied along the x-direction to drive the flow. Figure 3.1 illustrates the computation domain that was utilized for all simulations within this chapter.

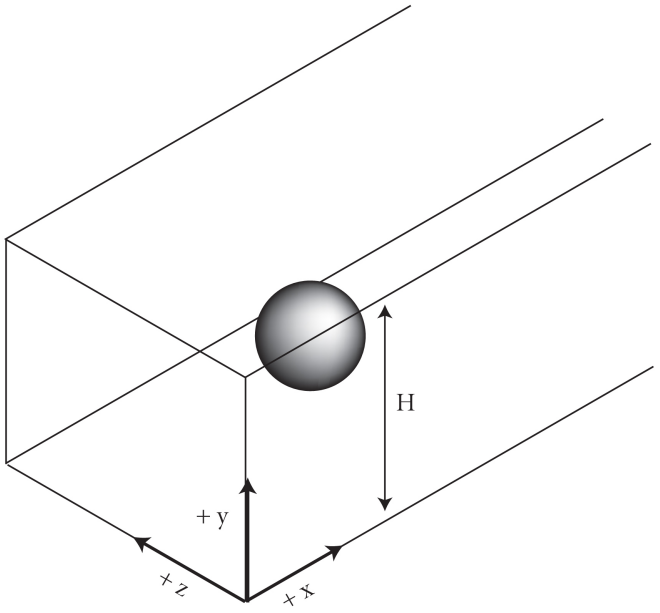

Figure 3.1. Channel compuational domain.

The neutrally buoyant capsule is modeled using the lattice spring method (LSM). The capsule is constructed with two shells/layers of lattice spring nodes with a distance of $0.28R$ apart. Each layer is comprised of 642 nodes. Between each node is a harmonic spring whose spring constant is set to achieve a desired Young's Modulus for the capsule. The spring constant k is determined by the equation,

$$k = \frac{2}{5}(E)(\Delta x_{LS}) \tag{52}$$

Where E is the Young's Modulus, k represents the spring constant, Δx_{LS} is the node spacing. This value of k is set for all spring-connected nodes on the surface and those normal to the surface. Diagonal springs are set for a value of $(2/3)k$.

The fluid is modeled using the lattice Boltzmann method (LBM). The system is setup such that the density is ρ=1 and the time setup is $\Delta t = 1$. The relaxation parameter is $\tau = 1$, which results in a fluid viscosity of $\nu = 1/6$. The same fluid viscosity is used within the fluid filled capsule. The flow is set into motion by imposing a body force that is proportional to the pressure gradient necessary to achieve the desired Reynolds number. The Reynolds number is varied between 10 and 40. The centerline velocity of the fluid by,

$$U_{\max} = \frac{H^2}{8\mu}\frac{dP}{dx} \tag{53}$$

The Reynolds number defined the same as Schonberg & Hitch in equation (1).

The simulations begin with a capsule of radius 10 in the center of the flow domain in the x- and z- directions. The y-position is a varied parameter where capsules are released at different positions within the channel in order to explore the impact of inertial drift in the micro-channel. The fluid and capsule are completely at rest at the initial time step.

3.3 Validation

The validation of the computational domain is necessary to ensure that the results produced are numerically accurate and consistent. As with most CFD, the grid needed to be validated that the results obtained from simulations converge on a solution. The verification of the computational grid is discussed in Section 3.3.1. Additionally, the model is validated against experiment in Section 3.3.2.

3.3.1 Grid Verification

The simulations discussed in this chapter explore the impact of deformation of soft capsules on the inertial drift of the capsule in micro-channel flow. The primary properties determined are both the equilibrium position of the capsule within the channel and the deformation of the capsule itself. Grid validation was performed to determine how the density of the grid affects the results obtained from simulations. The first validation step was exploring the impact of varying the grid resolution for rigid particles. This was accomplished by varying the channel radius and height, but leaving the ratio of the channel height to capsule diameter was 5. For example, a capsule with diameter of 8 was placed in a channel height 40 and a capsule with diameter of 24 was placed in a channel height of 120. Since the distance between lattice-Boltzmann nodes is set to 1, these channels have, respectively, 40 and 120 lattice-Boltzmann nodes between the opposing walls. The error normalized with the channel height is shown in Figure 3.2. The solution converges when the LBM nodes per capsule radius is larger than 8. This is assumed to be close to the correct resolution. In our simulations we use grids with 10 LBM nodes per capsule radius, which gives the error in the relative equilibrium position less than 0.05% of the channel height.

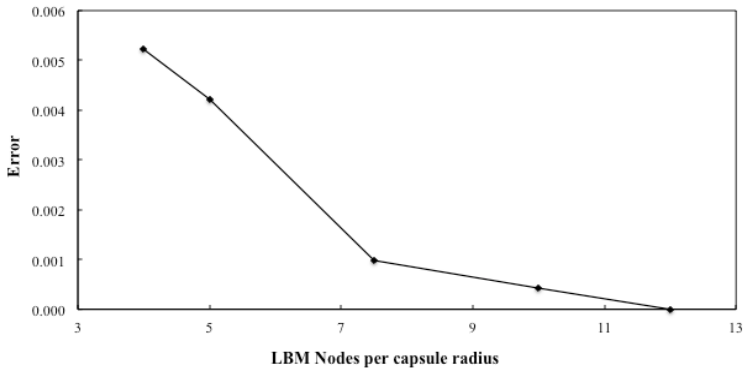

Figure 3.2. Position error of capsule while maintaining channel aspect ratio of 5.

3.3.2 Comparison with Schonberg & Hinch

The dynamic behavior was modeled for a capsule in a wide channel and compared the results with the theoretical results of [22]. A single rigid capsule was placed in different heights y/H within a channel. The heights were varied from 0.05 to 0.5. The simulation was set for a large channel H/a=60. After the capsule is released and reaches a steady motion, its cross-stream drift velocity is measured. The comparison between our results and the theoretical results from the literature is shown in Figure 3.3. We also use these simulations to find the capsule equilibrium position, which is the point where a capsule velocity approaches zero. The equilibrium position is determined by taking two near zero velocities with opposite directions and linearly interpolating between them.

Figure 3.3 shows that the capsule had drift velocities that change with the lateral distance from the wall. In this figure, the capsule lateral position is normalized by the channel height. When the capsule is near the wall, the capsule has a drift velocity towards the channel centerline. This is due to increased shear along the channel wall. When the capsule is far away from the wall and near the channel center, the capsule has a negative velocity due to the curvature in the parabolic velocity profile. Furthermore, the simulation predicts the capsule equilibrium position where the velocity is equal to zero at wall distance of 0.182. The theoretical value predicted by Schonberg is 0.185, a difference of just 1.6%. In addition, the simulation is capable of producing the same velocity curve predicted by [22].

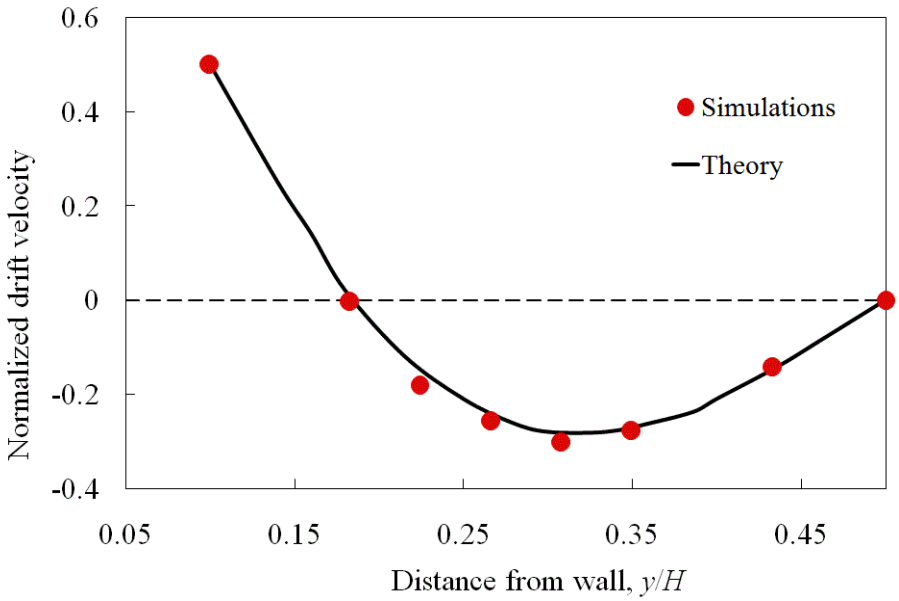

Figure 3.3. Comparison between theoretical predictions for equilibrium position with that computed by simulation.

3.4 Results and Discussion

A number of simulations were performed with rigid and soft capsules. The effect of the channel height and Reynolds number on inertial migration for rigid capsules and comparison with experimental results is discussed in Section 3.4.1. Additionally, soft capsules were explored to determine how varying system parameters such as channel height and Reynolds number impact the system. This is discussed further in Section 3.4.2. The relationship between the deformation and equilibrium position is discussed in Section 3.4.3.

The system can be characterized using the capillary number that relates the viscosity of the fluid to the stiffness of the capsule. The capillary number of the system is related to the deformation of the capsule in Section 3.4.4. Finally, the effects varying the

viscosity of the internal fluid of the capsule while keeping the outside fluid viscosity constant is explored in Section 3.4.5.

3.4.1 Effect of Channel Height on Inertial Migration for Rigid Capsules

One of the sorting parameters of interest is sorting particles and cells by size. The effect of varying the channel size relative to the capsule radius was explored using channel aspect ratios, H/a, ranging between 4 and 20. In particular, we study the influence of channel height on the inertial drift of the capsule and it's influence on the equilibrium position, y/H.

Figure 3.4 shows the normalized drift velocity with respect to the distance from the wall for different channel aspect ratios. The Reynolds number was kept a constant value of 10 for these simulations. Firstly, we find that the magnitude of normalized drift velocity decreases with decreasing aspect ratio. Secondly, the equilibrium position of the capsule is sensitive to the channel aspect ratio. As the channel aspect ratio increases, the equilibrium position moves closer to the channel wall. Thus, there is a clear relationship between the channel aspect ratio and the inertial drift velocity leading to changes in equilibrium positions. Therefore, rigid particles can be sorted based on their size relative to the channel height.

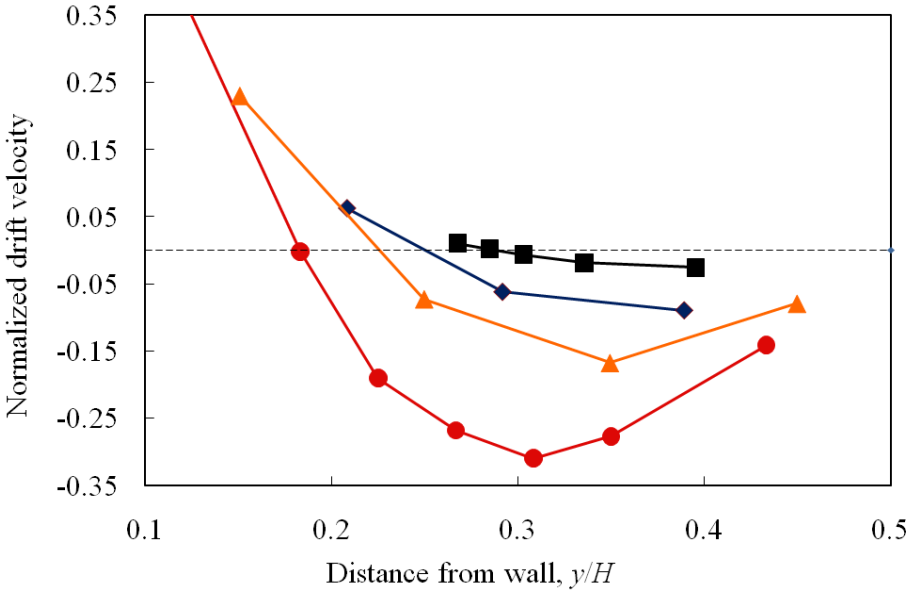

Figure 3.4. Normalized drift velocity as a function of wall distance for various channel height aspect ratios (*H*/*a*) for rigid capsules. They Reynolds number for the flow is 10. Each line represents a different channel height aspect ratio. The aspect ratios of each line are 5 (square), 10 (diamond), 20 (triangle), and 60 (circle).

In Figure 3.5, the equilibrium position is plotted as a function of the channel aspect ratio. We find that the equilibrium position approaches to the channel center line for narrow channels, and it is close to the predictions of [22] when the channel is wide, resulting in a large channel aspect ratio. In this figure, we also show how the equilibrium changes if the Reynolds number is increased to 40. The difference between curves for Re=10 and Re=40 is small, indicating that there is a weak dependency of inertial drift on Reynolds number.

This relationship between the channel aspect ration and equilibrium position has been experimentally verified. The Di Carlo group at UCLA provided the experimental data for the equilibrium position of droplets [36]. Oil droplets with an internal viscosity of 970 cP were submerged in water and released in the channel. At the outlet, the droplet equilibrium position was recorded using a Phantom v7.3 high speed camera. The samples

were injected using a syringe pump and had a flow rate of 25 µl/min to 450 µl/min. Due to the high viscosity the droplets maintained a nearly spherical shape during experiments. We performed simulations using a computational setup that matches the experimental setup. Specifically, the aspect ratio of the channel, 2:1, is the same as the experimental channel where the smaller side is the direction of migration of the capsule. Note that the experiment is at a Reynolds number of 20 while the simulation varies from 10 to 40.

There is close agreement between the results produced by our simulations and the experiment. Again, we find that the equilibrium position moves towards the centerline with a lower aspect ratio *H/a*. As the aspect ratio gets very large, we see that the equilibrium position approaches the theoretical results reported in [15] .

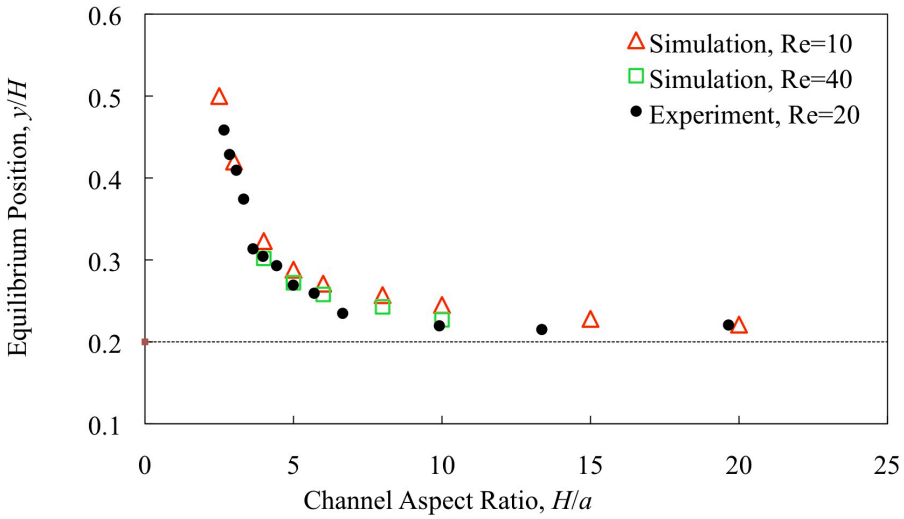

Figure 3.5. Comparison of equilibrium position of rigid capsules with experimental results.

This data of rigid capsules indicates that particles can be sorted based on their size using inertial drift. For example, suppose 10µm and 20 µm solid beads need to be sorted in a channel with a height of 100 µm. If the Reynolds number of the flow is 10, the 10

μm bead will have an equilibrium position of 23.5 μm from the wall. The larger bead will have an equilibrium position of 27.5 μm from the wall.

3.4.2 Effect of Channel Height on Inertial Drift for Soft Capsules

In Section 3.4.1, it was shown that the equilibrium position of rigid capsules moves away from the centerline of the channel for increasing heights. In this section, the equilibrium position of soft capsules is probed in a similar fashion. In order to measure the deformation of compliant capsules, the method of measuring deformation needs to be established. The deformation of compliant capsules can be difficult to quantify. While subject to the forces within the flow, the capsule is free to deform in any direction and rotate. Since the deformed capsule is commonly shaped similar to an ellipsoid, the change in geometry is quantified in those terms. This simplifies measurement of deformation and allows comparison with both theoretical and experimental results. The deformation is quantified using the following equation:

$$D = \frac{L_{max} - L_{min}}{L_{max} + L_{min}} \tag{54}$$

A detailed figure is shown below.

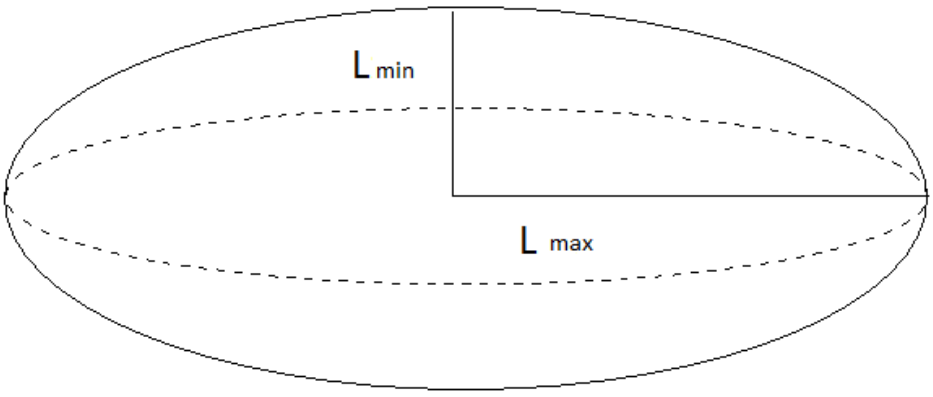

Figure 3.6. Ellipsoid geometry.

When a pressure gradient is imposed, the capsule begins moving along the channel. At the same time, the capsule moves normal to the channel wall with a cross-steam velocity proportional to the imposed Reynolds number of the flow. As with the rigid capsule, when the capsule approaches the wall, the capsule is subject to wall effects due to an increase in shear. The combination of inertial drift and shear forces drive the capsule to move towards the off-center equilibrium position. For deformable capsules, the increased shear near the wall results in a larger deformation. The deformation results in an increased lift force proportional to the level of deformation encountered.

In order to quantify the effect of the deformation on the equilibrium position, simulations were set up with soft capsules with compliance values. Compliance is defined by,

$$\Phi = \frac{4\mu^2}{\rho d G_s} \tag{55}$$

where G_s is the two-dimensional shear modulus,

$$G_s = \frac{0.5Eh}{(1+\nu)} \tag{56}$$

A flow was imposed with a Reynolds number of 10. The deformation and equilibrium position were determined for each capsule with different compliance. The results of these simulations are shown in Figure 3.7.

As with rigid capsules, increasing the channel height results in the capsule equilibrium position moving away from the centerline of the channel. Furthermore, the equilibrium position of soft capsules is closer to the centerline than the equilibrium position of rigid capsules. As the elasticity of the capsule decreases, the equilibrium position of the capsule moves closer to the centerline.

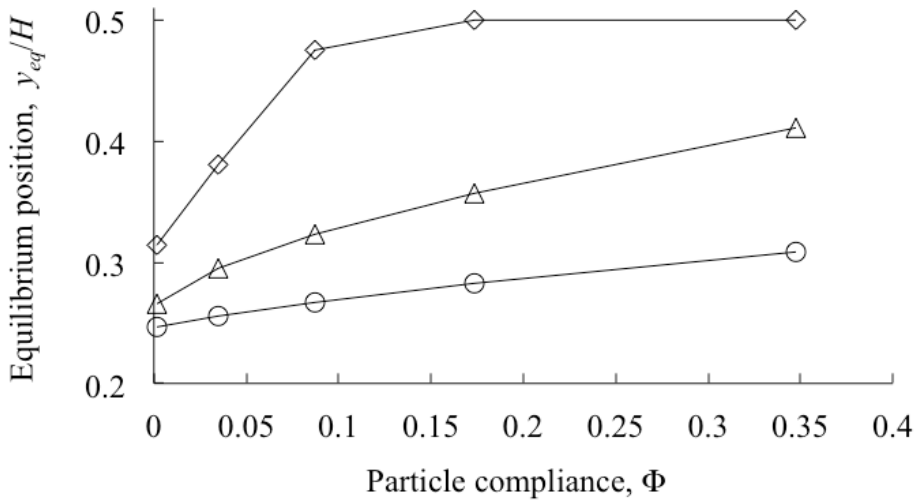

Figure 3.7. Equilibrium position as a function of particle compliance, *Φ*. Each line represents a channel aspect ratio *H/a* of 10 (circle), 6 (triangle), and 4 (diamond).

For the application of soft cell and particle sorting, a softer cell or particle of a similar size can be distinguished from another rigid particle. While not a sole indicator, cancer cells have a different stiffness than healthy cells [10]. The cells can be separated by their stiffness by submerging them into microfluidic flow so they may be further interrogated.

3.4.3 Effect of Deformation

In Section 3.4.2, the equilibrium position of soft capsules has been shown to vary from that of rigid capsules. Soft capsules have equilibrium positions closer to the channel centerline than rigid capsules. The differences between soft and rigid capsules can be attributed to the deformation that the soft capsules exhibit under viscous stresses while in the channel. When a soft capsule is near a wall, it is subject to an increased shearing rate that increases the deformation. If the Reynolds number is increased, this also increases

the shear in the flow causing the capsule to deform. The equilibrium position of the capsule is dependent on the deformation or shape of the capsule. Figure 3.8 shows the equilibrium position of soft capsules in relation to deformation calculated using equation (54) for Reynolds numbers 10 and 40. Figure 3.8 implies that when deformation increases, the equilibrium position within the channel moves towards the centerline.

Furthermore, as the Reynolds number is increased, the deformation of the capsule also increases. But, this increased deformation does not yield a higher equilibrium position as maybe expected. For example, in a channel with an aspect ratio of 10, the deformation is 0.01 for a Reynolds number of 10 and 0.032 for a Reynolds number of 40. The equilibrium position of these capsules is approximately the same.

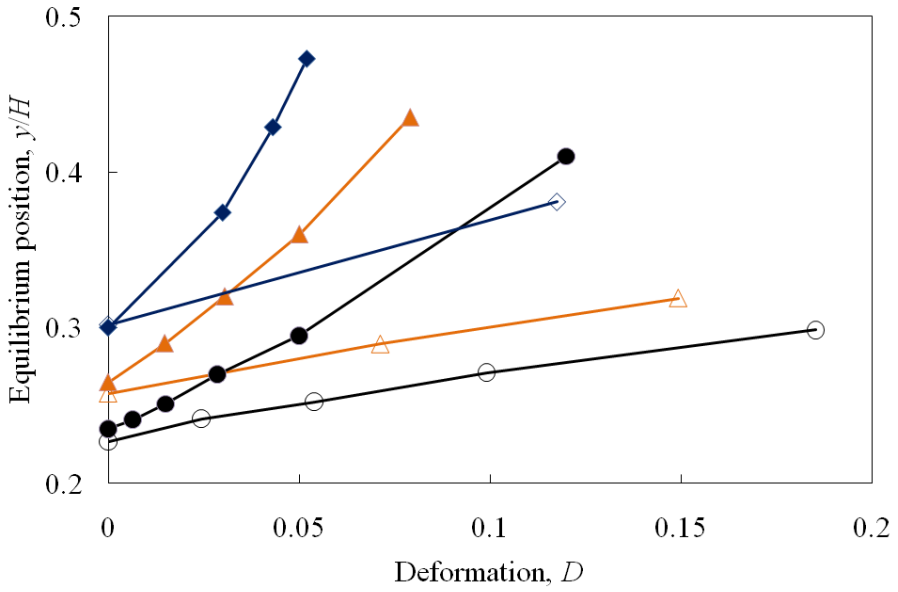

Figure 3.8. Comparison between equilibrium position for channel aspect ratio of 4 (diamond), 6 (triangle), and 10 (circle). Reynolds number equal to 10 (filled symbols) and 40 (unfilled symbols).

For further comparison, Figure 3.9 shows the equilibrium position of the capsule as a function of capsule compliance, Φ, for various Reynolds numbers. Firstly, this shows that equilibrium position stays the same, despite the capsule is more deformed in

that position at a higher Reynolds number. This implies capsule compliance, not shape defines the equilibrium position of the capsule. Secondly, we find that more compliance capsules migrate towards the channel centerline. Lastly, this figure implies that cells and synthetic particle cannot be distinguished by simply increasing the Reynolds number of the flow.

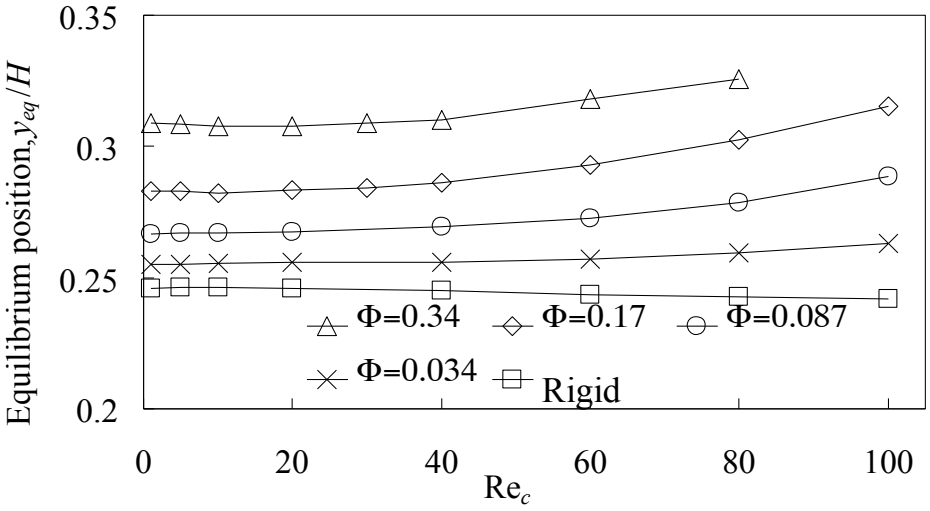

Figure 3.9. Particle equilibrium position as a function of particle compliance Φ for $\mathrm{Re}_c = 10$ and different particle aspect ratios A. The circles, triangles, and diamonds show data for *H/a*=10, 6, and 4, respectively.

3.4.4 Relationship Between Deformation and Capillary Number

The capillary number can be used to relate the dominance of the viscosity of the flow to the capsule compliance. While channel capillary number, Ca_c, can be utilized to characterize the system, the local capillary number is highly significant. The local capillary number, Ca_L, considers the local magnitude of the shear rate at the position of the capsule during simulation.

The relationship of the deformation and the local capillary number for a channel aspect ratio of 5 is shown in Figure 3.10. Furthermore, the deformation of a capsule is in pure shear is shown to be practically identical. Therefore, the non-uniformity of the flow

shear rate does not affect capsule shape in wide channels. We also find that the deformation of capsules is slightly smaller than that predicted by a linear theory for thin spherical shells in a shear flow [37] represented by the dashed line. This difference can be attributed to the effect of bending rigidity of elastic capsules that is included in our numerical model, but is not accounted for by the linear theory. Thus, we can expect that capsules with lower bending rigidity will experience slightly larger deformations and, therefore, may equilibrate somewhat closer to the channel centerline.

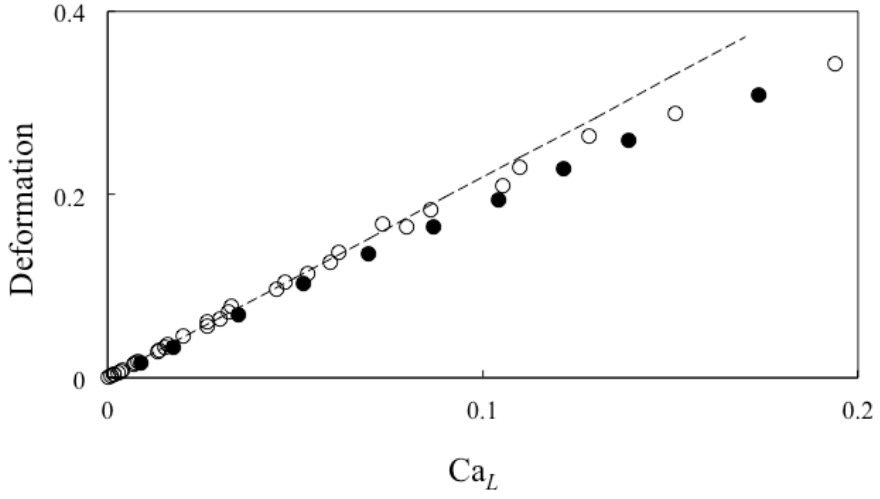

Figure 3.10. Capsule deformation for various local capillary numbers for channel aspect ratio, *H/a*=5. The empty symbols show the results for actual channel flow, while the filled symbols are for pure shear flow.

3.4.5 Equilibrium Position of Capsules with Different Viscosity Ratios

Simulations with soft capsules with different viscosity ratios were performed to examine the impact of the viscosity on the equilibrium position. A fluid-filled neutrally buoyant capsule was set up with a viscosity described by equation (35). Three different viscosity ratios, defined by the following equation, were used in the simulations.

$$\Gamma = \frac{\nu_c}{\nu_o} \tag{57}$$

Where Γ is the viscosity ratio, ν_c is the viscosity within the capsule, ν_o and is the viscosity of the outer fluid. The outer fluid's viscosity was kept at a constant value of 1/6 and the inner fluid viscosity was varied.

The relaxation parameter in equation (35) was varied such that the viscosity of the inner fluid was 2, 3, and 5 times larger than the viscosity of the outer fluid. The specific relaxation parameter, τ, is 1.5, 2, and 3.

The stiffness of the capsules was varied. The effect of the viscosity ratio is most prominent with the softest capsules. Simulations were run for an *Eh* range between 0.005 and 0.25. The capsule with *Eh*=0.005 was too soft resulting in the capsule collapse. Also, when the value of *Eh* was 0.05 and larger, the simulation yielded similar results to the prior case where the viscosities of the internal capsule and outer fluids were equal. This occurs because the deformation of the shell becomes insignificant and therefore the effect of internal fluid is less prominent. The three remaining *Eh* values are 0.0098, 0.015, and 0.025. The equilibrium position of the soft capsules with the viscosity ratios previously mentioned is shown in Figure 3.11.

This figure is plotted in terms of capillary number and shows its impact on the equilibrium position of the capsule for various viscosity ratios. As the capillary number is increased, the stiffness of the shell decreases. As was observed in section 3.3.5, increasing the capillary number results in larger deformation of the capsule. As previous data suggests, a larger deformation leads to the capsule approaching the centerline of the capsule.

Figure 3.11 shows that the viscosity of internal fluid has a profound impact on the equilibrium position. For low capillary numbers, the deformation of the capsules is relatively small, which results in small variation of the equilibrium position with viscosity ratio. However, as the capillary number increases, the increased deformation leads to a wider variation of equilibrium positions for a given capillary number. More specifically, as the viscosity ratio increases, the equilibrium position of the capsules moves away from the centerline of the channel. By increasing the viscosity ratio of the capsule, the deformation of capsule's shell is suppressed, which results in a capsule that behaves similar to one that is rigid.

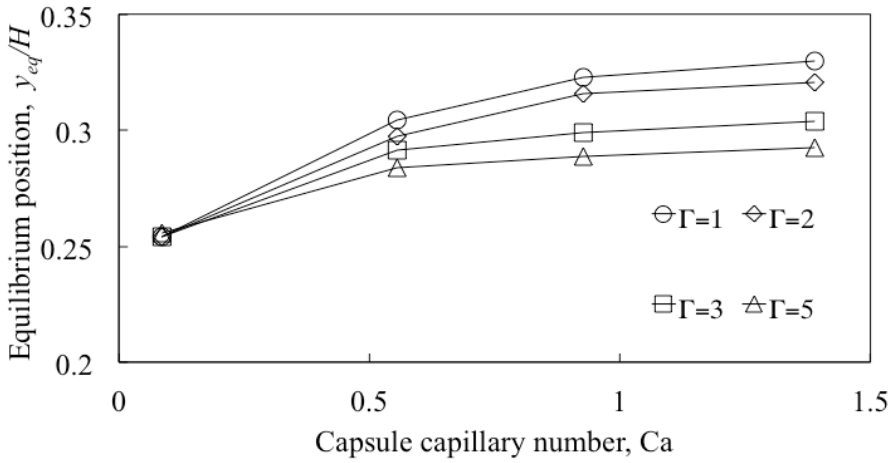

Figure 3.11. Equilibrium positions based on capsule capillary number for capsules of different viscosity ratio, Γ, for channel flow where Re=40.

3.5 Application of Inertial Migration to Cell Sorting

The data discussed in Section 3.4 show that capsules can be sorted by both size and stiffness. Furthermore, the data suggests that the equilibrium position of the capsules is independent of the flow rate. Therefore, the creation of a device to sort cells and synthetic particles based on their physical and mechanical properties is feasible. A proof-

of-concept device [13] that sort leukocytes and erythrocytes has been developed by the Di Carlo Laboratory is shown in Figure 3.12.

This device capitalizes on the phenomena discussed in Sections 3.4.1 and 3.4.2. The equilibrium position of the capsule is dependent on the channel size, where a large channel will produce more pronounced differences in equilibrium positions than smaller ones. The cells enter small channels upstream so that they become ordered and later interrogated to determine the cell type.

Figure 3.12(a) shows unordered cells entering a chamber and then separated into individual parallel micro-channels. As the cells progress downstream, the position of each cell will achieve an equilibrium position shown in Figure 3.12(b). Using inertial drift, the Di Carlo group has been able to differentiate cell types at a rate of 1,000,000 cells/sec using conventional microscopic analysis and high speed imaging [13].

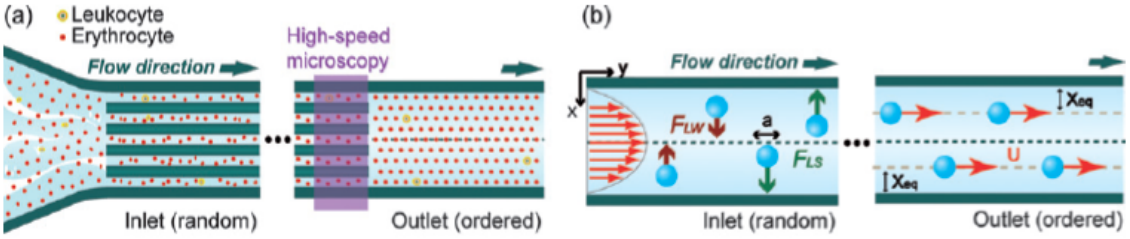

Figure 3.12: Di Carlo Experiment [13]. A group of unordered cells are sorted in channels (a) and reach an equilibrium position downstream of inlet (b).

CHAPTER 4

DROPLETS

4.1 Introduction

In the previous section, we have shown that capsule deformation has a significant influence on capsule cross-stream inertial migration. In this section we compare deformation of fluid filled capsules with liquid droplets in pure shear flow. This information may be useful for extending our results for deformable capsules to liquid droplets.

4.2 Computational Setup

The binary fluid model as described in Section 2.4 was used for simulations that involved liquid droplets. The droplet was placed in the center of a three dimensional channel between two walls moving in the opposite directions at a constant speed, *U*. The channel configuration is shown in Figure 4.1.

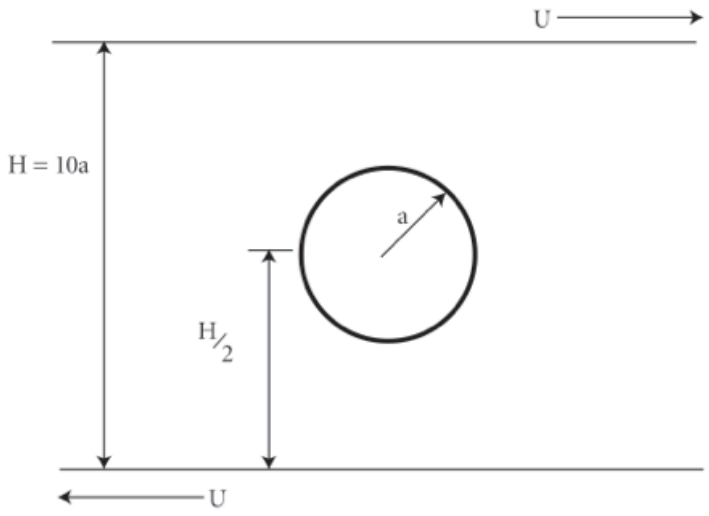

Figure 4.1. Computational setup for droplet subject to shear testing.

The droplet radius (a) for all tests remained a constant value of 10. The channel height (H) is equal to 100. The wall velocity was varied to set the required magnitude of the capillary number defined below. The capillary number is defined in terms of the shear rate (γ), the viscosity of the fluid (μ), and the surface tension of the droplet (σ).

$$Ca = \frac{\mu \gamma a}{\sigma} \tag{58}$$

The system parameters that govern the interface thickness and surface tensions were obtained from [33]. The specific values are shown in Table 1.

Table 1. Binary LBM Parameters

σ	a_{LBB}, b_{LBB}	κ	M
0.0083	0.00125	0.008	10
0.0021	0.00313	0.002	8
0.0042	0.00625	0.004	4
0.042	0.0625	0.04	0.5
0.055	0.083	0.053	0.1

4.3 Model Validation – Phase Separation

One of the validation tests was performed to verify the phase separation of a binary fluid. In this test, two fluids mixed throughout the domain. A random distribution of fluid was distributed across the entire domain with order parameters ranging from 1 (fluid A saturated) to -1 (fluid B saturated). The distribution was set such that the mean value of the order parameter was 0 across the domain signifying that there is an equal quantity both fluids in the domain as shown in Figure 4.2 (left).

The 3D domain size was 50 lattice Boltzmann units in each direction. There were 125,000 nodes total within the domain. Periodic boundary conditions were applied in all directions. The results of the simulation are shown in Figure 4.2 (right). As expected, the fluid begins to phase separate and begins to form a droplet.

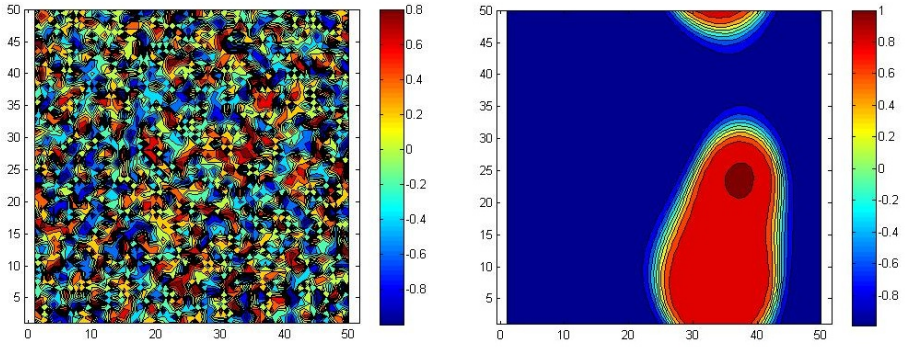

Figure 4.2. Two fluid phase separation test: Initial (left) and Final (right) state.

4.4 Model Validation – Shear Test

Testing was performed to validate the droplet in shear. The droplet is placed in a channel setup as described in Section 4.2. The initial state of the droplet is shown in Figure 4.3.

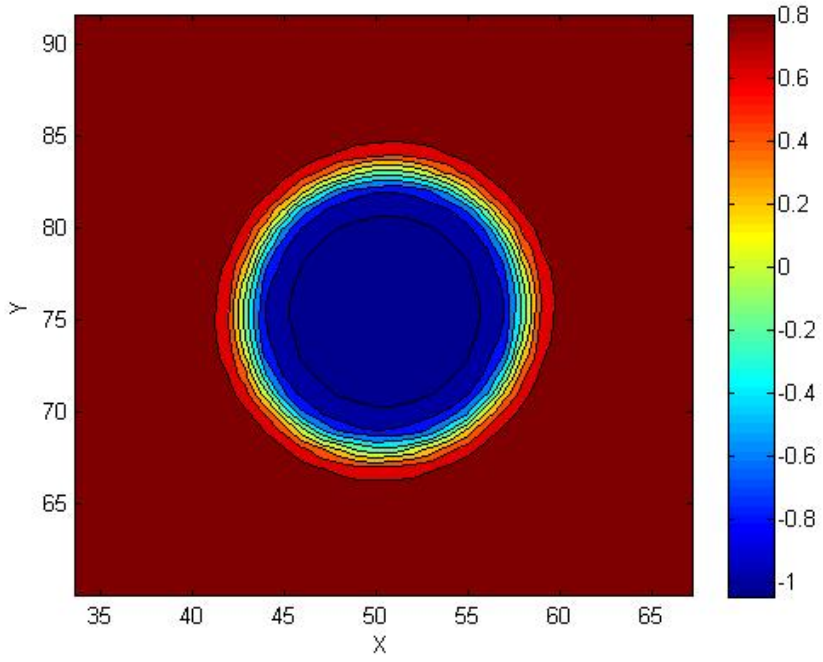

Figure 4.3. Droplet setup in channel. A region fully saturated with fluid A (red) has a value of 1, or fluid B (blue) with a value of -1.

According to [38], assuming a small deformation, the theoretical deformation of a droplet subject to shear is a function of the capillary number of the system. The theoretical deformation of the capsule is,

$$D = Ca\frac{19\mu_a + 16\mu_b}{16\mu_a + 16\mu_b} = \frac{L_{\max} - L_{\min}}{L_{\max} + L_{\min}} \tag{59}$$

The capillary number is defined in equation 58. The viscosity of fluid A and fluid B are defined as μ_a and μ_b, respectively. The dimensions L_{max} and L_{min} refer to the length of the semi-major and semi-minor axes of an ellipsoid. This definition matches the definition of the deformation of a capsule in equation (54). In the simulation, the viscosities of the fluid inside and outside the droplet were identical. In this case, the deformation for the droplet changes linearly as the capillary number increases.

$$D = Ca\frac{35}{32} \tag{60}$$

A 2-D (left) and 3-D (right) rendering of a capsule deformed 0.018 is shown in the following Figure 4.4.

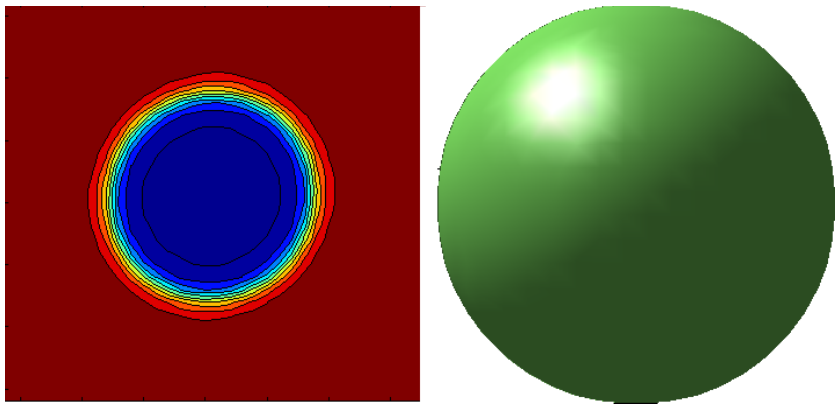

Figure 4.4. Rendering of droplet deformed by 1.8%. The 2D view (left) and 3D view (right) as shown.

The comparison between the theoretical results predicted by Taylor and that of the simulation are shown in Figure 4.5. The simulations produce results similar to that of the theory. This confirms that for capillary numbers below 0.1 the linear theory is sufficiently accurate to describe the deformation of droplets in shear flow.

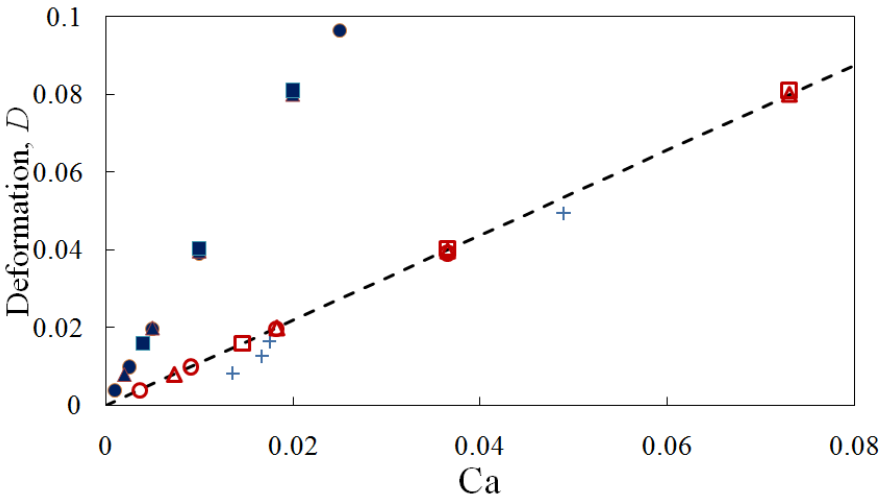

Figure 4.5. Comparison between droplet (plus sign) deformation produced by simulations and theoretical deformation (dotted line) predicted by [38]. Capsules are shown at different Reynolds number of 6 (circle), 12 (triangle), and 24 (square). The original data are represented by filled symbols and the adjusted data are shown by unfilled symbols.

4.5 Comparison Between Droplets and Capsules

The relationship between droplets and capsules needs to be established in order to attempt to translate the results for solid capsules to liquid droplets. Capsules and droplets both deform under shear. For small deformations, where the deformation is less than 0.1, the deformation of droplets is close to theory. For capsules, the deviation exceeds greatly the prediction of the theory developed for droplets. The comparison between the deformation of droplets and capsules as a function of capillary number is shown in Figure 4.5. This figure also shows the theoretical prediction.

As can be observed above, the difference between the capsule deformation and theory is significant. This is due to the difference in the definition of interfacial properties of droplets and capsules. We found however that this range of capillary numbers, the capsule deformation is independent of the Reynolds number.

In order to adjust for this difference, a correction factor was determined to match the results between capsules and droplets. The data for the capsule were correlated to that droplets and a line of best fit was determined. The adjusted data are also shown in Figure 4.5. In this case the capsule capillary number was multiplied by a correction factor given by:

$$C_{adj} = 3.65Ca \tag{61}$$

By correcting the capillary number for capsules to match the deformation of droplets, we can expect that the results for inertial migration of deformable capsules can be used to estimate the effect of inertial migration of droplets with a comparable deformability characterized by capillary number.

CHAPTER 5

CONCLUSIONS & FUTURE WORK

5.1 Conclusions

The effect of inertial drift on equilibrium position of capsules subject to laminar Poiseuille flow in microchannels has been explored under a number of conditions. The impact of system parameters such as the Reynolds number, capillary number, and channel height has also been quantified. The data obtained from the simulations can be potentially extended to droplets using a correction factor that translate deformation of capsules and droplets with identical capillary numbers defining their compliance.

It is found that the equilibrium position for rigid capsules is weakly dependent on the channel Reynolds number. The primary method to control the equilibrium position of rigid capsules is to change the channel aspect ratio, either by adjusting the size of the capsule or the channel height. By keeping the capsule radius fixed and increasing the channel height, the capsule moves further away from the channel centerline. Conversely, by decreasing the channel height, the capsule equilibrium position moves closer to the channel center. For the purposes of sorting rigid capsules by size in channel flow, it is expected that the small capsules will be further away from the channel centerline.

For soft capsules, the equilibrium position depends on both capsule elasticity and channel height. As observed with the rigid capsules, the capsules move closer to the centerline with a smaller channel aspect ratio. Since the soft capsules are free to deform, the deformation has an impact on the equilibrium position as well. For softer capsules, the deformation is greater which results in the capsules moving closer the channel centerline. When the Reynolds number is varied, the equilibrium position stays

approximately the same. But, the deformation at that equilibrium position is higher for larger Reynolds numbers.

This data suggests that cells and synthetic particles can be focused by their properties with equipment sensitive enough to detect the differences in equilibrium position. It can be used to differentiate cell types by size and stiffness. Further research needs to be done on exploring wider ranges of channels and Reynolds numbers. Furthermore, droplet models need to be enhanced so that the inertial drift velocity and equilibrium position can be quantified in a similar manner to capsules.

5.2 Future work

In this thesis, the affect of capsule compliance on inertial drift velocity and equilibrium position was explored. It was observed that the softer capsules achieved an equilibrium position closer to the channel centerline than rigid particles. One of the observations obtained was that the capsule stiffness, not Reynolds number, is the governing factor in driving the equilibrium position closer to the channel centerline. This effect is observed across Reynolds numbers 1-100. This implies that forces that set the equilibrium position scale similarly with the Reynolds number. The importance of understanding these forces is critical in a further understanding of how the stiffness impacts the lift of the capsule.

Further exploration is necessary to determine the impact of capsule concentrations on the capsule equilibrium position. This thesis is limited to dilute systems. An understanding of capsule-capsule interactions is necessary for the development of devices with high concentrations of cells or synthetic particles.

A major assumption for all simulations was the capsule was spherical and undeformed at the start of the simulations. Additional research exploring capsules that have non-spherical shapes is necessary to determine the impact on inertial drift.

Additionally, this thesis attempted to relate the deformation of droplets to the results obtained from capsules. Additional work is necessary to strengthen this relationship. This includes repeating the simulations performed in Chapter 3 with droplets instead of capsules.

REFERENCES

1. Huh, D., et al., *Microfluidics for flow cytometric anlysis of cells and particles.* Physiological Measurement, 2005(Volume 26, Number 3).
2. Hans, M.L. and A.M. Lowman, *Biodegradable nanoparticles for drug delivery and targeting.* Current Opinion in Solid State and Materials Science, 2002. **6**(4): p. 319-327.
3. Brannon-Peppas, L., *Recent advances on the use of biodegradable microparticles and nanoparticles in controlled drug delivery.* International Journal of Pharmaceutics, 1995. **116**(1): p. 1-9.
4. Di Carlo, D., et al., *Continuous inertial focusing, ordering, and separation of particles in microchannels.* Proceedings of the National Academy of Sciences, 2007. **104**(48): p. 18892-18897.
5. Huh, D., et al., *Gravity-Driven Microfluidic Particle Sorting Device with Hydrodynamic Separation Amplification.* Analytical Chemistry, 2007. **79**(4): p. 1369-1376.
6. Sulchek, T.A., A. Alexeev, and G. Wang, *Microfluidic Device for Separation of Particles*, U.S.P.a.T. Office, Editor 2010, Georgia Tech Research Corporation: United States. p. 5.
7. Cross, S.E., et al., *Nanomechanical analysis of cells from cancer patients.* Nat Nano, 2007. **2**(12): p. 780-783.
8. Guck, J., et al., *Optical Deformability as an Inherent Cell Marker for Testing Malignant Transformation and Metastatic Competence.* Biophysical Journal, 2005. **88**(5): p. 3689-3698.
9. Suresh, S., *Biomechanics and biophysics of cancer cells.* Acta Biomater, 2007. **3**(4): p. 413-438.
10. Suresh, S., et al., *Connections between single-cell biomechanics and human disease states: gastrointestinal cancer and malaria.* Acta Biomaterialia, 2005. **1**(1): p. 15-30.
11. eBioScience, I. *Cell Preparation for Flow Cytometry*. 2009 [cited 2011 01/14/2011]; Available from: http://www.ebioscience.com/ebioscience/appls/pdf/cell-preparation-flow-cytometry-staining.pdf.
12. Greig, B., et al., *2006 Bethesda International Consensus recommendations on the immunophenotypic analysis of hematolymphoid neoplasia by flow cytometry: Recommendations for training and education to perform clinical flow cytometry.* Cytometry Part B: Clinical Cytometry, 2007. **72B**(S1): p. S23-S33.
13. Hur, S.C., H.T.K. Tse, and D. Di Carlo, *Sheathless inertial cell ordering for extreme throughput flow cytometry.* Lab on a Chip, 2010. **10**(3): p. 274.
14. Segré, G. and A. Silberberg, *Behaviour of macroscopic rigid spheres in Poiseuille flow Part 1. Determination of local concentration by statistical analysis of particle passages through crossed light beams.* Journal of Fluid Mechanics, 2006. **14**(01): p. 115.
15. Segré, G. and A. Silberberg, *Behaviour of macroscopic rigid spheres in Poiseuille flow Part 2. Experimental results and interpretation.* Journal of Fluid Mechanics, 2006. **14**(01): p. 136.

16. Cox, R.G. and H. Brenner, *The lateral migration of solid particles in Poiseuille flow -- I theory.* Chemical Engineering Science, 1968. **23**(2): p. 147-173.
17. Leal, L.G., *Particle Motions in a Viscous Fluid.* Annual Review of Fluid Mechanics, 1980. **12**(1): p. 435-476.
18. Matas, J., J. Morris, and E. Guazzelli, *Lateral Forces on a Sphere.* Oil & Gas Science and Technology, 2004. **59**(1): p. 59-70.
19. Koh, C.J., P. Hookham, and L.G. Leal, *An experimental investigation of concentrated suspension flows in a rectangular channel.* Journal of Fluid Mechanics, 2006. **266**(-1): p. 1.
20. Rubinow, S.I. and J.B. Keller, *The transverse force on a spinning sphere moving in a viscous fluid.* Journal of Fluid Mechanics, 1961. **11**(03): p. 447.
21. Ho, B.P.a.L., L.G., *Inertial Migration of rigid spheres in two-dimensional unidirectional flows.* Journal of Fluid Mechanics, 1974. **65**.
22. Schonberg, J.A. and E.J. Hinch, *Inertial migration of a sphere in Poiseuille flow.* Journal of Fluid Mechanics, 2006. **203**: p. 517.
23. Verberg, R., J.M. Yeomans, and A.C. Balazs, *Modeling the flow of fluid/particle mixtures in microchannels: Encapsulating nanoparticles within monodisperse droplets.* The Journal of Chemical Physics, 2005. **123**(22): p. 224706.
24. Alexeev, A., R. Verberg, and A.C. Balazs, *Modeling the motion of microcapsules on compliant polymeric surfaces.* Macromolecules, 2005. **38**(24): p. 10244-10260.
25. Bouzidi, M., M. Firdaouss, and P. Lallemand, *Momentum transfer of a Boltzmann-lattice fluid with boundaries.* Physics of Fluids, 2001. **13**(11): p. 3452-3459.
26. Gunstensen, A., et al., *Lattice Boltzmann model of immiscible fluids.* Physical Review A, 1991. **43**(8): p. 4320-4327.
27. Inamuro, T., *A lattice Boltzmann method for incompressible two-phase flows with large density differences.* Journal of Computational Physics, 2004. **198**(2): p. 628-644.
28. Ladd, A.J.C. and R. Verberg, *Lattice-Boltzmann Simulations of Particle-Fluid Suspensions.* Journal of Statistical Physics, 2001. **104**(5/6): p. 1191-1251.
29. Luo, L.-S. and S. Girimaji, *Lattice Boltzmann model for binary mixtures.* Physical Review E, 2002. **66**(3): p. 035301.
30. Orlandini, E., M.R. Swift, and J.M. Yeomans, *A Lattice Boltzmann Model of Binary-Fluid Mixtures.* Europhysics Letters (EPL), 1995. **32**(6): p. 463-468.
31. Swift, M.R., et al., *Lattice Boltzmann simulations of liquid-gas and binary fluid systems.* Physical Review E, 1996. **54**(5): p. 5041.
32. Aidun, C.K. and J.R. Clausen, *Lattice-Boltzmann Method for Complex Flows.* Annual Review of Fluid Mechanics, 2010. **42**(1): p. 439-472.
33. Kendon, V.M., et al., *Inertial effects in three-dimensional spinodal decomposition of a symmetric binary fluid mixture: a lattice Boltzmann study.* Journal of Fluid Mechanics, 2001. **440**.
34. Missirlis, Y. and M. Brain, *An improved method for studying the elastic properties of erythrocyte membranes.* Blood, 1979. **54**(5): p. 1069-1079.
35. Needham, D., *A sensitive measure of surface stress in the resting neutrophil.* Biophysical Journal, 1992. **61**(6): p. 1664-1670.

36. Kilimnik, A., et al., *Cross-stream migration of compliant particles in microfluidic channels*, in *63rd Annual Meeting of the APS Division of Fluid Dynamics* 2010: Long Beach, CA.
37. Barthès-Biesel, D., *Capsule motion in flow: Deformation and membrane buckling.* Comptes Rendus Physique, 2009. **10**(8): p. 764-774.
38. Taylor, G.I., *The Formation of Emulsions in Definable Fields of Flow.* Proceedings of the Royal Society A: Mathematical, Physical and Engineering Sciences, 1934. **146**(858): p. 501-523.